

## Article

# Flow Behavior and Microstructure of Hot-Worked Fe-30.9Mn-4.9Al-4.5Cr-0.4C and Fe-21.3Mn-7.6Al-4.3Cr-1C Low-Density Stainless Steels

Takatso Komane, Nthabiseng Maledi, Desmond Klenam , Josias van der Merwe and Michael Bodunrin \* 

School of Chemical and Metallurgical Engineering, University of the Witwatersrand, Johannesburg 2050, South Africa

\* Correspondence: michael.bodunrin@wits.ac.za; Tel.: +27-11-717-7506

**Featured Application:** Automotive and Bio-implant applications.

**Abstract:** Two as-cast low-density steels grades (austenite-based duplex Fe-30.9Mn-4.9Al-4.5Cr-0.4C and austenitic Fe-21.3Mn-7.6Al-4.3Cr-1C) with an initial dendritic microstructure were subjected to hot working conditions to understand the influence of deformation parameters on flow behavior and microstructural evolution. The alloys were produced using electric arc melting, and their phase constituents were determined using optical microscopy and X-ray diffraction analysis. This was then corroborated with the phase predicted from Thermo-Calc simulation. The as-cast alloys were machined to  $10 \times 10 \times 7$  mm specimen configurations for rectangular axial testing on the Gleeble 3500 thermomechanical simulator. The samples were deformed to a total strain of 0.5 at different deformation temperatures (800, 900, and 1000 °C) and strain rates (0.1 and 5 s<sup>-1</sup>). Thereafter, a hardness test was conducted on the deformed samples, and post-deformed microstructures were analyzed using optical and scanning electron microscopes. The results showed that the alloys' dendritic structures were effectively transformed at temperatures below 1000 °C regardless of the strain rate. At all deformation conditions, the peak flow stress of Fe-21.3Mn-7.6Al-4.3Cr-1C alloy was at least 50% higher than that of Fe-30.9Mn-4.9Al-4.5Cr-0.4C alloy owing to the higher carbon content in the austenitic low-density stainless steel. The hardness of all the deformed samples was superior to that of the as-cast samples, which indicates microstructural reconstitution and grain refinement in the alloys. Dynamic recrystallization, dynamic globularization, and dynamic recovery influenced the softening process and the microstructural changes observed in the alloys under different deformation conditions.

**Keywords:** lightweight steels; thermomechanical processing; dynamic recovery; dynamic recrystallization; Gleeble 3500



**Citation:** Komane, T.; Maledi, N.; Klenam, D.; van der Merwe, J.; Bodunrin, M. Flow Behavior and Microstructure of Hot-Worked Fe-30.9Mn-4.9Al-4.5Cr-0.4C and Fe-21.3Mn-7.6Al-4.3Cr-1C Low-Density Stainless Steels. *Appl. Sci.* **2023**, *13*, 2310. <https://doi.org/10.3390/app13042310>

Academic Editor: Guijun Bi

Received: 13 January 2023

Revised: 6 February 2023

Accepted: 8 February 2023

Published: 10 February 2023



**Copyright:** © 2023 by the authors. Licensee MDPI, Basel, Switzerland. This article is an open access article distributed under the terms and conditions of the Creative Commons Attribution (CC BY) license (<https://creativecommons.org/licenses/by/4.0/>).

## 1. Introduction

The need to minimize fuel consumption in automobile engines and ultimately reduce greenhouse gas emissions contributed by the transportation industry has resulted in the development of a wide range of light alloys with high specific strength and crashworthiness. Low-density steels remain one of the light alloys that have received significant attention from researchers in the last decade owing to their attractive combination of properties, such as high strength, good balance between ductility and toughness, good fatigue strength, good oxidation and corrosion resistance, and high energy absorption under impact loading [1,2]. These outstanding mechanical properties could benefit a whole range of other industries, such as the cryogenic and construction industries. This is because different property combinations can be obtained in low-density steels by manipulating process parameters and microstructural control [3].

The different property combinations exhibited by low-density steels were accomplished by adding lightweight elements such as Al, Ti, Si, and C into the Fe-Mn alloy system, reducing the density and increasing the strength-to-weight ratio [2]. The alloying elements in low-density steels yield various microstructures that either complement the material's integrity if added in the right amounts or degrade it when added in excess [3]. For example, the presence of Mn in high amounts promotes the stability of the preferred austenite phase. In addition, the presence of other alloying elements such as Al, Cr, and C in controlled amounts precipitates intragranular carbides, such as K-carbides,  $M_{23}C_6$ ,  $M_7C_3$ , and  $M_3C$ , which are responsible for the different strengthening mechanisms observed in these alloys [2,4,5]. However, with high Al content (>9%), a disordered ferrite containing ordered B2 and DO3 phases is likely to nucleate along the grain boundaries, and these phases embrittle low-density steels [3]. Furthermore, high Al and C additions may result in the formation of intergranular K-carbides that also reduce the ductility of low-density steels. Of all the alloying elements in low-density steels, Al is considered the most important as it yields a ~1.3% reduction in density per one weight percent (wt%) of Al, but the elastic modulus reduces considerably with increasing Al content [1,3,4]. Owing to the sensitivity of low-density steels to slight compositional changes, there have been considerable research efforts on phase calculation and alloy development to understand the formation of phases and how they influence the properties of the different grades of low-density steels.

These research efforts have led to classifying low-density steels based on their microstructural constituents [3,4]. Typical microstructures of low-density steels have matrices that can be austenitic ( $\gamma$ ), ferritic ( $\alpha$ ), or duplex ( $\alpha + \gamma$ ). Precipitates of different carbides can also form in the matrices depending on the constituent elements, their amount, and processing conditions [3]. The most promising low-density steel is the austenitic Fe-Mn-Al-C type owing to its excellent combination of properties [4]. Consequently, more attention has been given to this grade of low-density steels. In 2020, Moon et al. [5] developed new grades of austenitic low-density steels by adding different amounts of Cr into the conventional Fe-Mn-Al-C system. They found that ~5 wt% Cr was optimum to yield high ductility without significantly compromising strength. These alloys also exhibited a superior pitting potential in 3.5 wt% NaCl medium compared to conventional stainless steels. These Cr-bearing low-density steels were dubbed low-density stainless steels [5]. While the two main authoritative reviews published in 2017 [4] and 2021 [3] on low-density steels have concluded that these alloys are very promising for automotive, structural, and cryogenic applications, they pointed out that they have hardly been used in the aforementioned applications because of several reasons, including low elastic modulus, processing problems associated with high Al and Mn content, and the limited experimental results on formability, weldability, and coatability.

Despite this, the authors of this work have considered the low elastic modulus and light weight of low-density steels as attractive properties for biomedical applications. Additionally, the amenability to conventional processing techniques and cheap manufacturing costs would validate the exploration of low-density steels as alternative bio-implant materials. Therefore, by building on the findings of Moon et al. [5], we hypothesized that some grades of Cr-bearing low-density steels could be promising for orthopedic implant applications. This served as the basis for studying Fe-30.9Mn-4.9Al-4.5Cr-0.4C and Fe-21.3Mn-7.6Al-4.3Cr-1C low-density stainless steels.

The use of stainless steels in the biomedical industry is not a new concept; it was first used in the 1920s, and its success paved the way for treating human bone fractures [6,7]. Some common metallic biomaterials of preference are AISI 316L stainless steels, Co-Cr alloys, and Ti-6Al-4V alloys [8]. The limitations of these common orthopedic implant alloys include the high cost and toxicity of Co-Cr and Ti-6Al-4V alloys and the high density of AISI 316L stainless steels ( $8.03 \text{ g/cm}^3$ ) compared to the density of human cortical bone ( $0.96$  to  $1.9 \text{ g/cm}^3$ ) [9]. Low-density stainless steels considered in this study may replace expensive titanium alloys, and highly dense 316L stainless steel should have good corrosion resistance. Consequently, a preliminary corrosion investigation was conducted on different

compositions of as-cast low-density stainless steels immersed in simulated body fluids (0.9 wt% NaCl and Hanks Balanced Salt Solution). Their corrosion rates were compared with AISI 316L stainless steel exposed to the same solutions. The as-cast low-density stainless steels had a dendritic structure with carbides forming at the inter-dendritic region of the austenite matrix [10]. The results show that the two alloys of focus in this study have a lower corrosion rate than commercial-grade AISI 316L stainless steel in simulated body fluids. However, they were still susceptible to pitting corrosion, localized in the interdendritic region of as-cast low-density stainless steels (see Supplementary Figure S1).

Bosch et al. [11] also reported pitting corrosion in their austenitic Fe-Mn-Al-Cr-C steels in NaCl and NaOH solutions. However, the composition and microstructure of their alloys differ from those presented in this study. Prior to corrosion studies, their alloys were subjected to thermal treatment so that their starting microstructure had an equiaxed morphology. In addition to uniform corrosion, uniformly distributed pits were seen in the alloys owing to the dissolution of Fe and Mn. Their findings differ from ours in that pitting corrosion occurred preferentially at the carbide–austenite interface and the interdendritic regions.

Therefore, we envisaged that the corrosion performance of the two low-density stainless steels, Fe-30.9Mn-4.9Al-4.5Cr-0.4C and Fe-21.3Mn-7.6Al-4.3Cr-1C, could be enhanced further if the as-cast dendritic structure is broken down using thermomechanical processing techniques. Gutierrez-Urrutia [3] reported that microstructural control is necessary for property optimization in Fe-Mn-Al-C alloys. However, as the response of Fe-30.9Mn-4.9Al-4.5Cr-0.4C and Fe-21.3Mn-7.6Al-4.3Cr-1C alloys to deformation parameters has not been previously reported, it is important to understand their hot working behavior. While their compositions may fall within the broad groups of austenitic and austenite-based duplex low-density steels reported previously [4], the sensitivity of their response to compositional changes when subjected to different testing conditions has made it important to investigate the flow behavior and microstructural evolution in these alloys under hot working conditions. Chen et al. [4] and Ding et al. [12] reported that for low-density stainless steel to realize its potential as structural materials, more studies focusing on alloy development, strengthening mechanisms, corrosion studies, and workability at cold and hot working conditions are essential.

Therefore, this study sought the combination of thermomechanical processing parameters that would effectively break the dendritic structure in the as-cast Fe-30.9Mn-4.9Al-4.5Cr-0.4C and Fe-21.3Mn-7.6Al-4.3Cr-1C low-density stainless steels. This was performed by exploring these alloys' strain-hardening and softening behavior to understand their deformation-induced microstructures better [13]. The typical range of safe parameters for hot working of most Fe-Mn-Al-C low-density steels was used in this study to confirm whether they are suitable or not for the two alloys. The results could guide metallurgists in selecting appropriate parameters for the large-scale processing of these alloys for manufacturing biomedical components.

## 2. Materials and Methods

As-cast Fe-30.9Mn-4.9Al-4.5Cr-0.4C and Fe-21.3Mn-7.6Al-4.3Cr-1C low-density stainless steels were produced by melting compacted powders of pure elements that constitute the alloys in an electric arc furnace. The alloys were turned and melted three times to homogenize them. The chemical composition of the alloys was confirmed using an optical emission spectrometer. Thereafter, Thermo-Calc modeling was performed to predict the likely equilibrium phases in the alloys and the critical transformation temperatures. The amount of the alloying elements in mass percent was entered into the Thermo-Calc software using the TCFe8 thermodynamic database. X-ray diffraction (XRD) analysis was performed on the alloys using a Bruker D2 Phaser diffractometer. The XRD scan was performed at 2 $\theta$  angles of 10 to 90°. The measurements were taken at ambient temperature using generator settings of 10 mA, 30 kV, and cobalt as the anode material. The XRD patterns were matched using PANalytical software.

For thermomechanical testing, the alloys were machined into rectangular test samples of  $10 \times 10 \times 7$  mm configurations before subjecting them to rectangular axial isothermal compression testing on a Gleeble 3500 thermomechanical simulator. A platinum-rhodium (R-type) thermocouple was then welded to the mid-span of the samples. Nickel paste and graphite foil were applied in between the tungsten carbide ISO-T anvils and the samples to minimize frictional effects on the flow curves. Figure 1 shows the thermomechanical processing schedule applied to the samples. Three deformation temperatures of 800, 900, and 1000 °C and two strain rates of 0.1 and 5.0 s<sup>-1</sup> for each temperature were used. These parameters were selected from previous studies [13–15] and were considered safe for the hot working of Fe-Mn-Al-C low-density steels. Prior to deformation, the samples were heated at a rate of 5 °C/s up to a reheating temperature of 1200 °C and then soaked for 120 s to achieve homogenization at the reheating temperature. Thereafter, the samples were cooled to the deformation temperature at a rate of 1 °C/s and held for 60 s before deformation. All the samples were deformed to a total strain of 0.5 followed by compressed air quenching. The stress–strain data were then captured and analyzed.

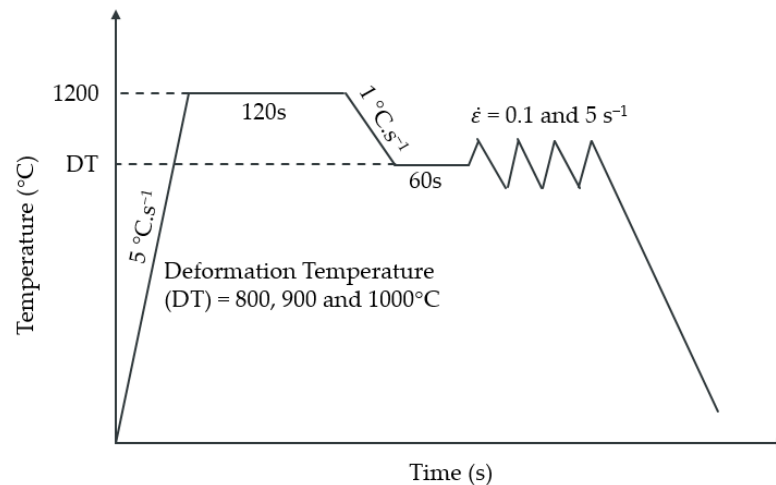


**Figure 1.** Hot working schedule for testing Fe-Mn-Al-Cr-C-based low-density steels.

For microstructural analyses, the deformed samples were sectioned into two halves parallel to the compression axis. One of each sample was mounted in an OPAL 410 mounting machine using a polyfast hot mounting resin. The mounted samples were then ground using an IMPTECH 201 grinding machine using silicon carbide abrasive paper of 800 to 2000 grit. They were polished with an alumina suspension and etched with Vilella's reagent. Microstructural observation of the polished samples was performed using both optical and scanning electron microscopes (SEM). The undeformed samples were prepared following a similar procedure. The obtained micrographs were then compared to observe the microstructural evolution that each sample went through under different deformation conditions.

To determine if there is a significant influence of deformation parameters on the hardness of the alloys, Vickers hardness testing was conducted using an FM 700 microhardness tester in accordance with ASTM E 92-17 [16]. The indentation was obtained by using a load of 500 gf and a dwell time of 15 s. An average hardness was computed from five measurements taken at random spots on each sample.

### 3. Results

#### 3.1. Initial Microstructure and Thermo-Calc Results

The initial microstructure of the two low-density stainless steels investigated in this study is presented in Figure 2. The two alloys had a fully dendritic structure with two distinct phases. Fe-30.9Mn-4.9Al-4.5Cr-0.4C is an austenite-based duplex low-density stainless steel with ferrite and austenite phases, while Fe-21.3Mn-7.6Al-4.3Cr-1C is an

austenitic low-density steel with dendritic carbide in an austenite matrix. Considering the classification of the two alloys, the composition of the alloys and their corresponding microstructures are consistent with the classification prescribed by Chen et al. [4] for austenitic low-density steels and austenite-based duplex low-density steels. However, the composition of the austenite-based duplex low-density steel in this work (Fe-30.9Mn-4.9Al-4.5Cr-0.4C) differs slightly from the classification prescribed by Guierrez-Urrutia [3]. Guierrez-Urrutia [3] reported that the Mn content in austenite-based duplex low-density steel varies between 10 and 25%, and the carbon content varies between 0.6 and 1.0%. In this work, Fe-30.9Mn-4.9Al-4.5Cr-0.4C has 30% Mn and 0.4% C; these values are only consistent with the work of Chen et al. [4]. The microstructural evidence in Figure 2a shows that the classification of low-density steels by Chen et al. [4] is more accurate.

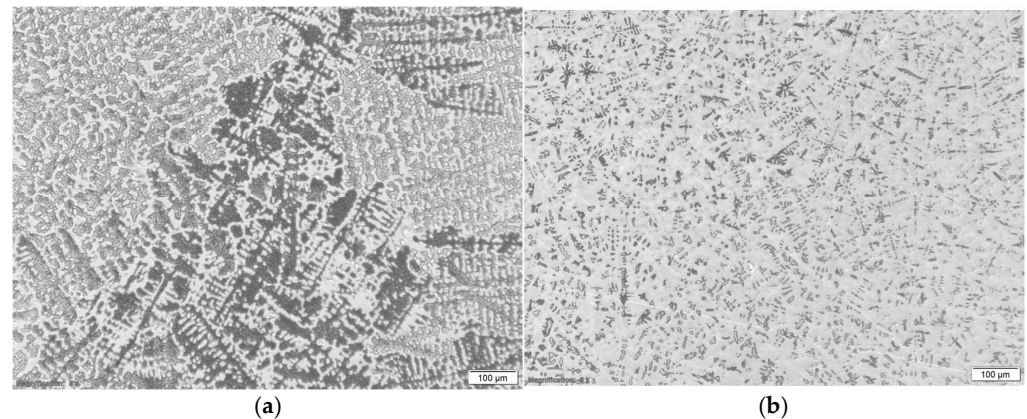


**Figure 2.** Initial microstructure of (a) Fe-30.9Mn-4.9Al-4.5Cr-0.4C; (b) Fe-21.3Mn-7.6Al-4.3Cr-1C.

Figure 3 presents the Thermo-Calc predictions showing the alloys' expected equilibrium phases. Below the solidus,  $\alpha$ -Fe (bcc),  $\gamma$ -Fe (fcc), and  $M_{23}C_6$  carbide are expected in Fe-30.9Mn-4.9Al-4.5Cr-0.4C alloy, while  $\alpha$ -Fe (bcc),  $\gamma$ -Fe (fcc), and carbides of  $M_7C_3$  and  $M_{23}C_6$  are expected in Fe-21.3Mn-7.6Al-4.3Cr-1C alloy under equilibrium conditions. However, the prominent peaks in the XRD patterns (Figure 4) confirmed the presence of  $\gamma$ -Fe (fcc) and  $Cr_7C_3$  ( $M_7C_3$ ) in both alloys. Ferrite and  $M_{23}C_6$  phases were not identified in either alloy. This could be due to the low volume fraction of the  $M_{23}C_6$  phase in the alloys. XRD cannot detect phases less than two volume percent [17]. In addition, a longer XRD scan may have picked up the ferrite phase in Fe-30.9Mn-4.9Al-4.5Cr-0.4C alloy.

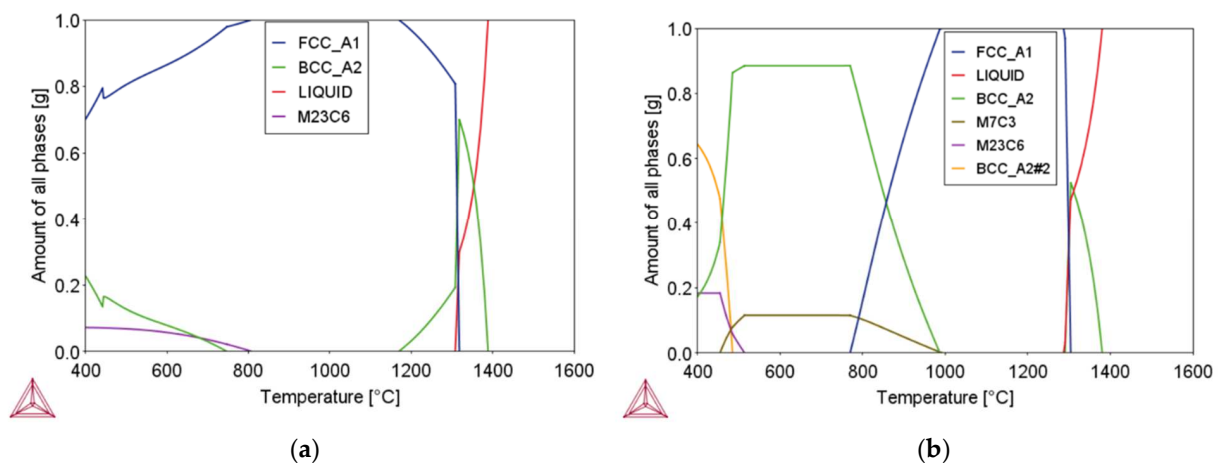


**Figure 3.** Phase prediction from Thermo-Calc for (a) Fe-30.9Mn-4.9Al-4.5Cr-0.4C; (b) Fe-21.3Mn-7.6Al-4.3Cr-1C.

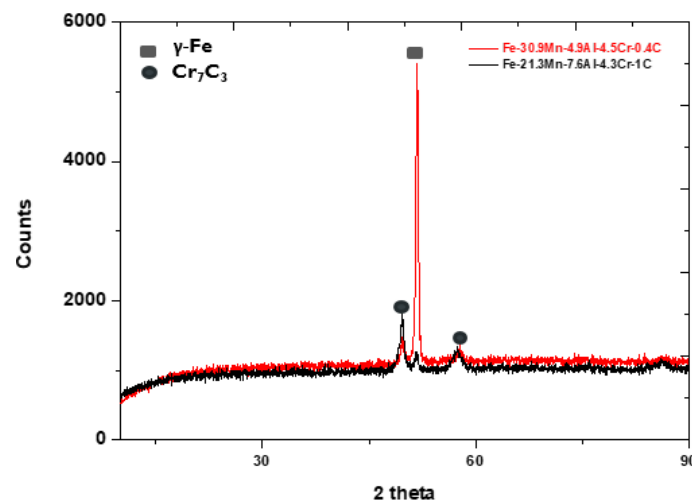


**Figure 4.** X-ray diffraction pattern of Fe-30.9Mn-4.9Al-4.5Cr-0.4C and Fe-21.3Mn-7.6Al-4.3Cr-1C low-density steels.

### 3.2. Flow Behavior and Hardness

The flow stress curves in Figure 5 were obtained from hot compression tests on the Gleeble using deformation temperatures (800, 900, and 1000 °C) and strain rates (0.1 and 5 s<sup>-1</sup>). The flow stress was sensitive to both the deformation temperature and strain rate. As expected in materials with positive strain rate sensitivity, the flow stress increased with increasing strain rate and decreasing deformation temperature [13,18]. Generally, it is reported that when low-density steels are subjected to hot working, the flow stress is higher at low temperatures and high strain rates, while it is lower at high temperatures and low strain rates [2]. The curves show that the flow stress increased drastically at the beginning of deformation until a peak stress, after which the softening effects on flow stress became obvious. The initial increase in flow stress depicts the dominance of work hardening [13–15]. This metallurgical phenomenon is controlled by the relationship between dislocation mean free path and dislocation length [19]. The work hardening rate is increased by decreasing the mean free path of dislocations [20]. The decrease in the mean free path depends on dislocation density and grain size; therefore, higher strain rates increase dislocation density while smaller grain size increases grain boundary area. Therefore, the mean free path of dislocation is decreased by high dislocation density and small grain size, causing dislocation motion impediment [19].

The flow stress curves show varying softening trends for the different testing conditions, suggesting that multiple softening mechanisms may have influenced the deformation process. It has been reported that the flow behavior of low-density steels is influenced by softening mechanisms such as continuous dynamic recrystallization, discontinuous dynamic recrystallization (DDRX), dynamic precipitation of intragranular K-carbides, and dynamic recovery [13]. Dynamic recrystallization (DRX) causes grain refinement, and the DRX grains' nucleation generally begins at a critical strain just before the peak stress is reached [21]. As seen in Figure 5a,b, the curves at 0.1 s<sup>-1</sup> strain rate show a rough flow oscillation depicting the possible occurrence of DDRX [22]. Luton and Sellars [23] focused on the mechanical aspect of DRX and reported that oscillating flow stress or cyclic flow stress are signatures of DDRX, but depending on the deformation temperature and strain rate, the multiple peaks for oscillating flow stress may transform to a single peak. Similar to the observation in Figure 5a,b, they emphasized that flow oscillations are expected at low strain rates and high deformation temperatures. Sakai and Jonas [24] later advanced this by looking at the microstructural aspect of DRX, establishing that flow oscillations with multiple peaks are related to the ratio of the initial grain size and the size of a stable dynamically recrystallized grain. In the case of flow oscillations, they showed that the initial grain size is less than the stable dynamically recrystallized grain and, for that reason, grain

coarsening occurs during deformation until the size of a stable dynamically recrystallized grain is reached.

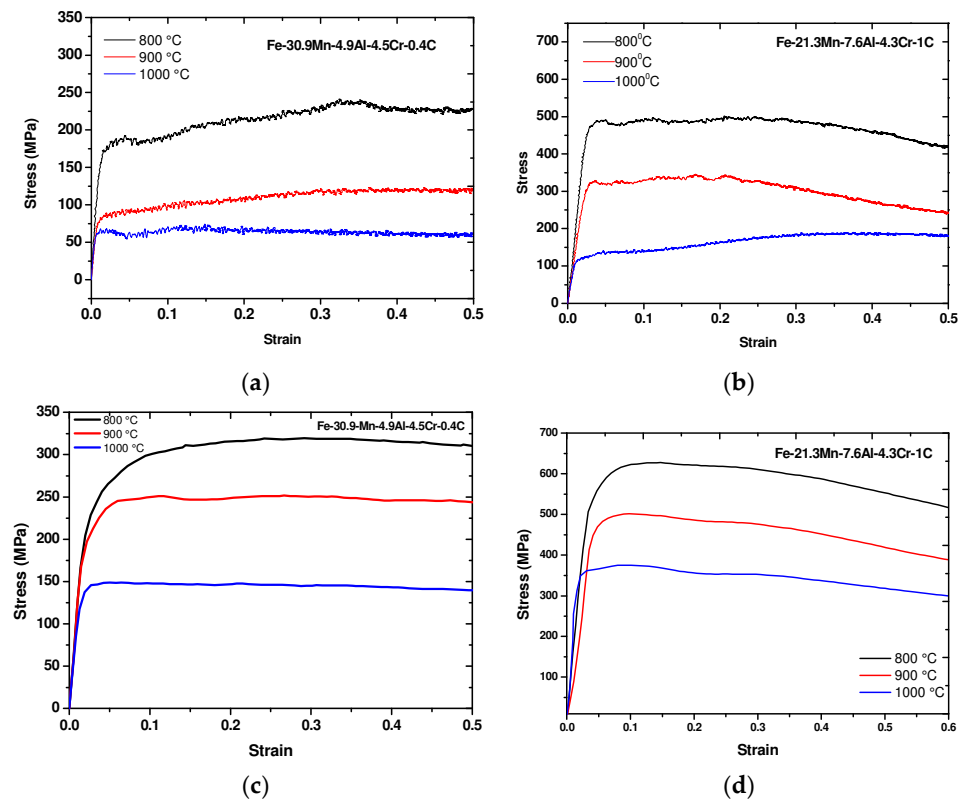


**Figure 5.** Flow stress at different deformation temperatures for Fe-30.9Mn-4.9Al-4.5Cr-0.4C (Sample A) at (a) 0.1 s<sup>-1</sup> and (c) 5 s<sup>-1</sup>; Fe-21.3Mn-7.6Al-4.3Cr-1C (Sample B) at (b) 0.1 s<sup>-1</sup> and (d) 5 s<sup>-1</sup>.

DRX appeared to be the dominating softening mechanism at a low strain rate because there is more time for the nucleation of new grains and grain growth. The flow stress at 800 and 900 °C declined continuously after peak stress and the strain exceeded 0.2 (Figure 5b), indicating continuous flow softening. This observed trend portrays a possible occurrence of deformation-induced defects, such as cracking or, in other instances, resulting from geometric dynamic recrystallization (GDRX), otherwise known as dynamic globularization, where elongated grains are transformed to a globular morphology [25,26].

When deformation was performed at a strain rate of 5 s<sup>-1</sup> (Figure 5c,d), a steady-state flow stress (Figure 5c) or a gradual decrease in flow stress (Figure 5d) was observed after the peak stress was attained. The steady-state flow stress suggests that dynamic recovery is the dominant softening mechanism controlling deformation under these conditions. As reported by Rodrigues et al. [27] using low-density stainless steels, at the initial stage of deformation, thermally activated mechanisms delayed the onset of DRX where there is competition between dynamic recovery and work hardening just before the peak stress is reached. Thereafter, dynamic recovery can balance work hardening, and a plateau of flow stress is accomplished as strain increases [21]. The microstructural analysis presented in Section 3.3 helps to confirm the occurrence of the various softening mechanisms (dynamic recovery or G/DRX) suggested by the observable trends on the flow curves in this section.

The flow stress of the two low-density steels was compared. Under all deformation conditions, Fe-21.3Mn-7.6Al-4.3Cr-1C exhibited higher flow stress than Fe-30.9Mn-4.9Al-4.5Cr-0.4C. This is quite conspicuous in the extracted peak stresses presented in Figure 6. The higher flow stress of Fe-21.3Mn-7.6Al-4.3Cr-1C showed that it is more difficult to deform than Fe-30.9Mn-4.9Al-4.5Cr-0.4C. However, if the alloy were to be used for higher-temperature applications, it offers superior high-temperature strength, which could be attributed to the higher carbon content in the Fe-21.3Mn-7.6Al-4.3Cr-1C alloy. The higher

carbon content suggests that more carbon atoms might be available for forming carbide precipitates in the alloy, and these precipitates are effective in impeding dislocation movement. The Vickers hardness results (Figure 7) show that there was no significant difference in the hardness of both alloys regardless of the deformation condition. For each alloy, the hardness was slightly sensitive to increasing deformation temperature but not to increased strain rate. The hardness values obtained after deforming the alloys were significantly higher than the hardness of the alloys ( $327 \pm 24$  for Fe-30.9Mn-4.9Al-4.5Cr-0.4C and  $464 \pm 18$  for Fe-21.3Mn-7.6Al-4.3Cr-1C) in the as-cast condition. The increase in hardness in the deformed alloys points to the breakdown of the dendritic structures and grain refinements. This is confirmed in Section 3.3.

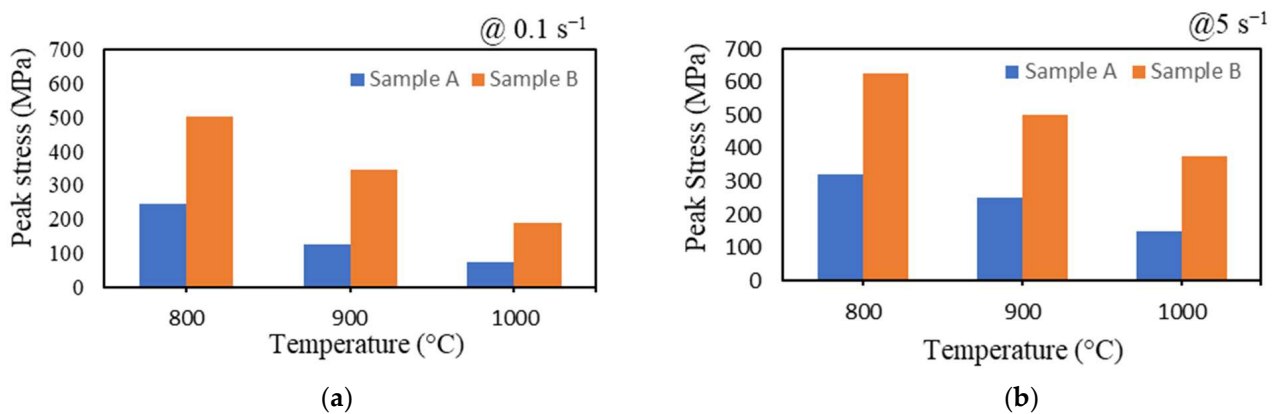


**Figure 6.** Extracted peak stresses from flow curves for alloys Fe-30.9Mn-4.9Al-4.5Cr-0.4C (Sample A) and Fe-21.3Mn-7.6Al-4.3Cr-1C (Sample B) deformed at different temperatures and constant strain rates of (a)  $0.1 \text{ s}^{-1}$ ; (b)  $5 \text{ s}^{-1}$ .

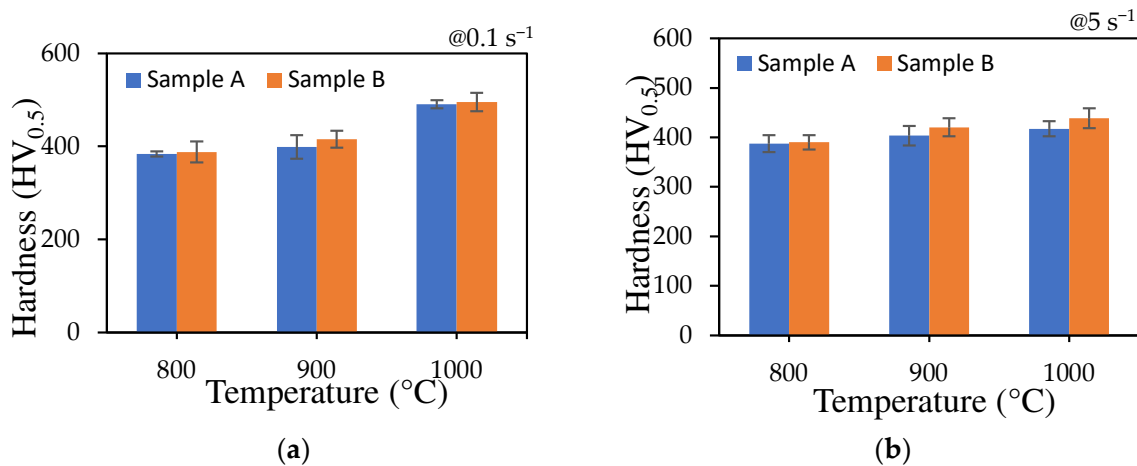


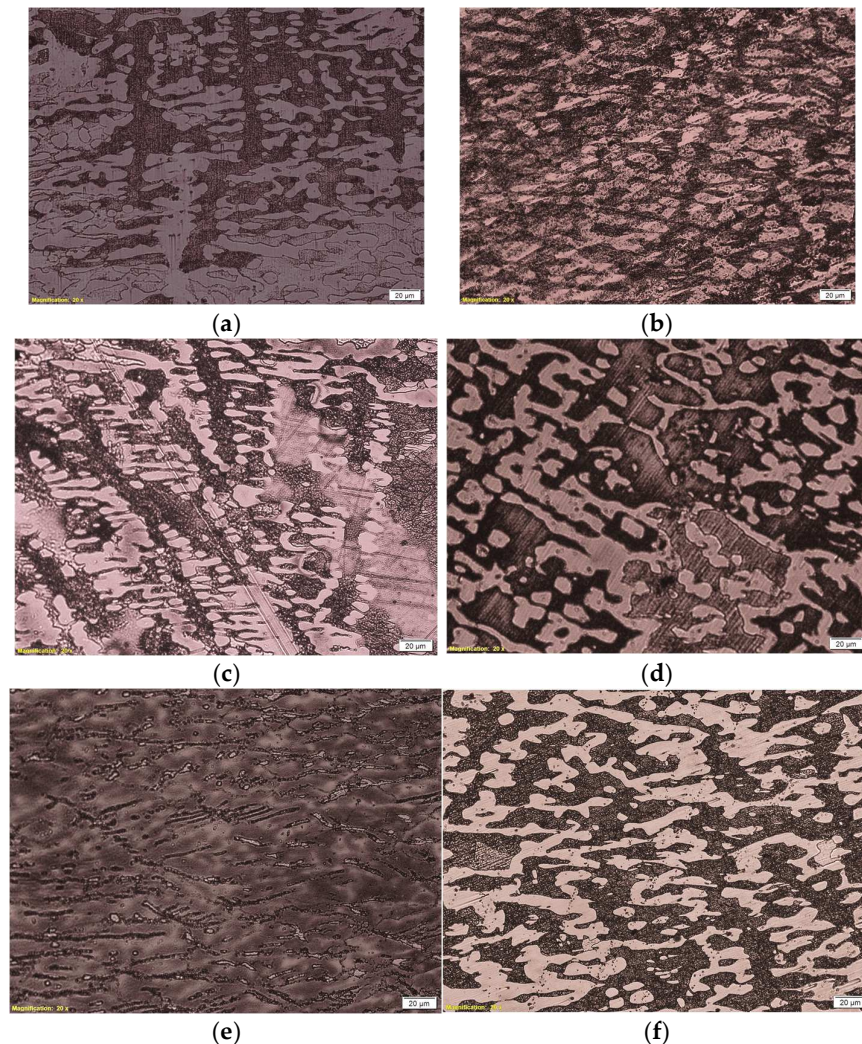
**Figure 7.** The hardness of Fe-30.9Mn-4.9Al-4.5Cr-0.4C (Sample A) and Fe-21.3Mn-7.6Al-4.3Cr-1C (Sample B) deformed at different temperatures and constant strain rates of (a)  $0.1 \text{ s}^{-1}$ ; (b)  $5 \text{ s}^{-1}$ .

### 3.3. Microstructural Evolution

#### 3.3.1. Optical Micrographs

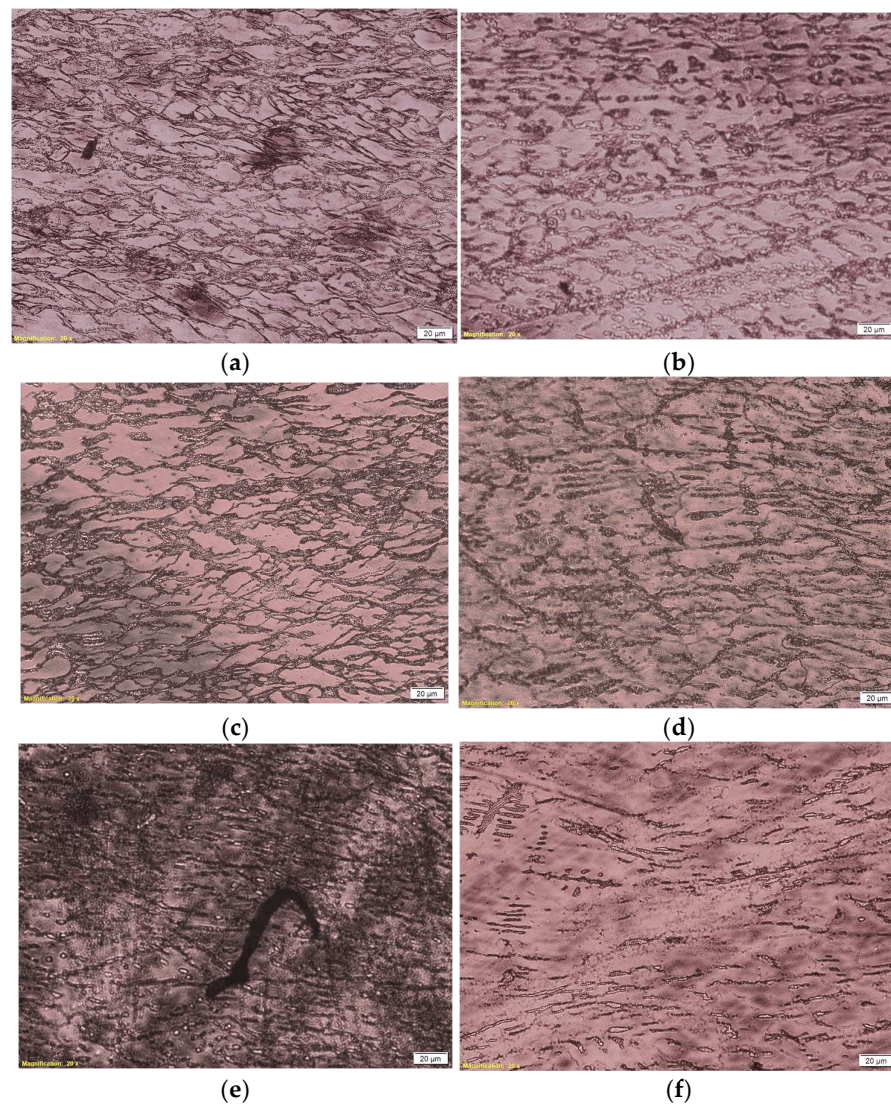
Figure 8 presents the optical micrographs obtained after Fe-30.9Mn-4.9Al-4.5Cr-0.4C was deformed. Deformation temperature and strain rate played a significant role in the evolution of the alloy's microstructure. Figure 8a,c show that at 800 and 900 °C and a strain rate of  $0.1 \text{ s}^{-1}$ , the fully dendritic structure in the as-cast alloy evolved into elongated and globular ferrite grains. At 1000 °C and  $0.1 \text{ s}^{-1}$  (Figure 8e), the dendritic features were eliminated, and strands of carbide ( $M_7C_3$ ,  $M_3C$ ,  $M_{23}C_6$ , or Kappa) phase embedded within the serrated austenite matrix were observed. In addition, the phase fraction of the ferrite phase depleted significantly. The depletion of the ferrite phase under this condition can be

ascribed to the low strain rate applied at a higher temperature allowing enough time for phase transformation to occur. Figure 8b,d,f also show the elongated and globular austenite grains with no distinct dendritic feature at all deformation temperatures and a constant strain rate of  $5 \text{ s}^{-1}$ .



**Figure 8.** Optical micrographs of deformed Fe-30.9Mn-4.9Al-4.5Cr-0.4C under different deformation conditions: (a) 800 °C at  $0.1 \text{ s}^{-1}$ ; (b) 800 °C at  $5 \text{ s}^{-1}$ ; (c) 900 °C at  $0.1 \text{ s}^{-1}$ ; (d) 900 °C at  $5 \text{ s}^{-1}$ ; (e) 1000 °C at  $0.1 \text{ s}^{-1}$ ; (f) 1000 °C at  $5 \text{ s}^{-1}$ .

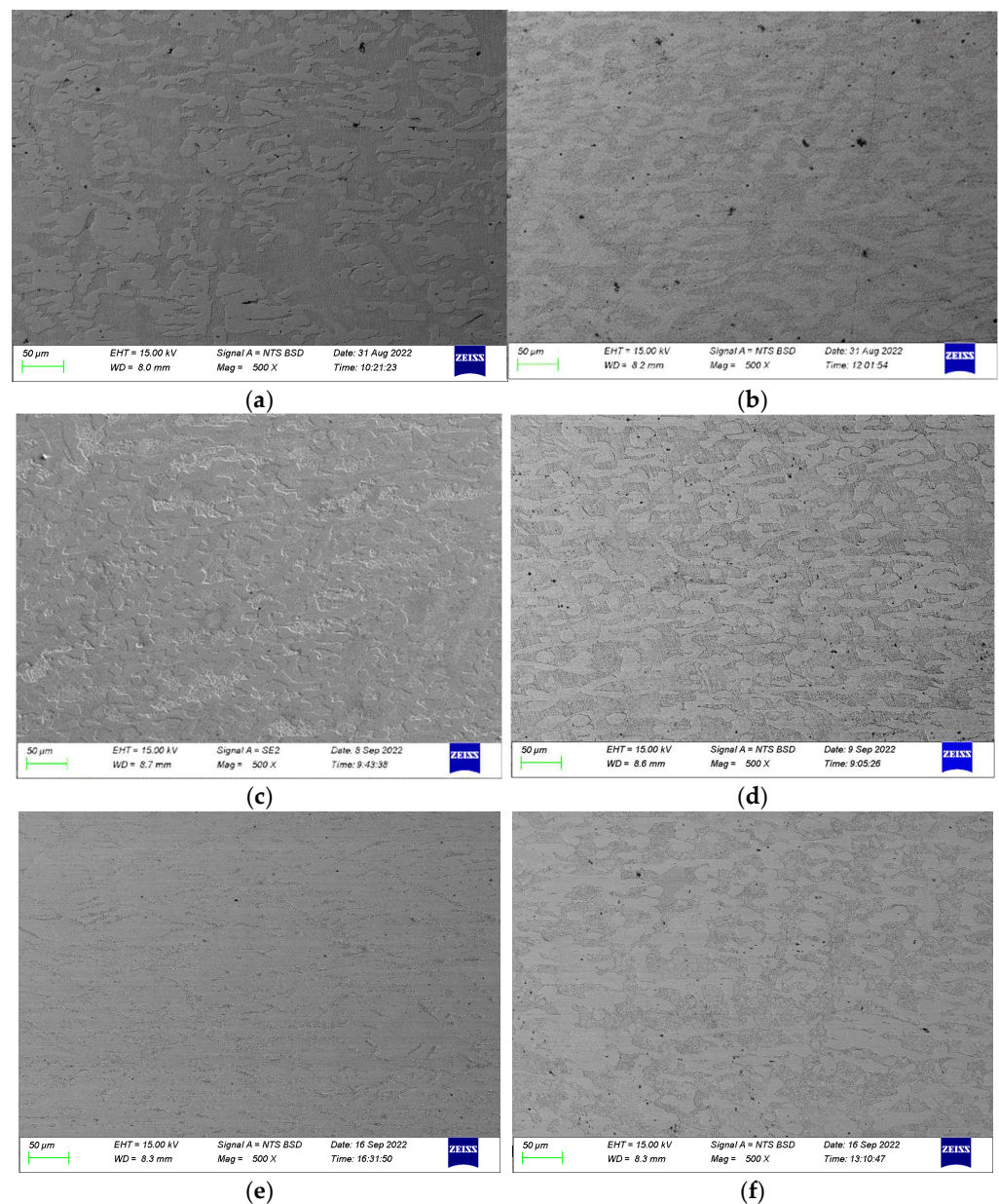
Similar to the Fe-30.9Mn-4.9Al-4.5Cr-0.4C austenitic-based duplex low-density steel, Fe-21.3Mn-7.6Al-4.3Cr-1C austenitic low-density steel followed the same response to changing deformation parameters in terms of the disappearance of the as-cast dendritic structure in the deformed samples under all conditions except at 1000 °C at  $5 \text{ s}^{-1}$  (Figure 9f) where dendritic features were still observed. At all strain rates and deformation temperatures below 1000 °C (Figure 9a–d), serrated austenite grains with a network of intergranular carbides ( $M_7C_3$ ,  $M_3C$ ,  $M_{23}C_6$ , or Kappa) were evident. Some of these austenite grains had a near-globular morphology. These serrated grains are signatures of dynamic recovery dominating at the onset of DRX [28–30]. The near-globular morphology confirmed the occurrence of the small amount of dynamic globularization, as suggested by the continuous flow softening in Figure 6b.



**Figure 9.** Optical micrographs of deformed Fe-21.3Mn-7.6Al-4.3Cr-1C under different deformation conditions: (a) 800 °C at  $0.1 \text{ s}^{-1}$ ; (b) 800 °C at  $5 \text{ s}^{-1}$ ; (c) 900 °C at  $0.1 \text{ s}^{-1}$ ; (d) 900 °C at  $5 \text{ s}^{-1}$ ; (e) 1000 °C at  $0.1 \text{ s}^{-1}$ ; (f) 1000 °C at  $5 \text{ s}^{-1}$ .

### 3.3.2. Scanning Electron Microscope Images

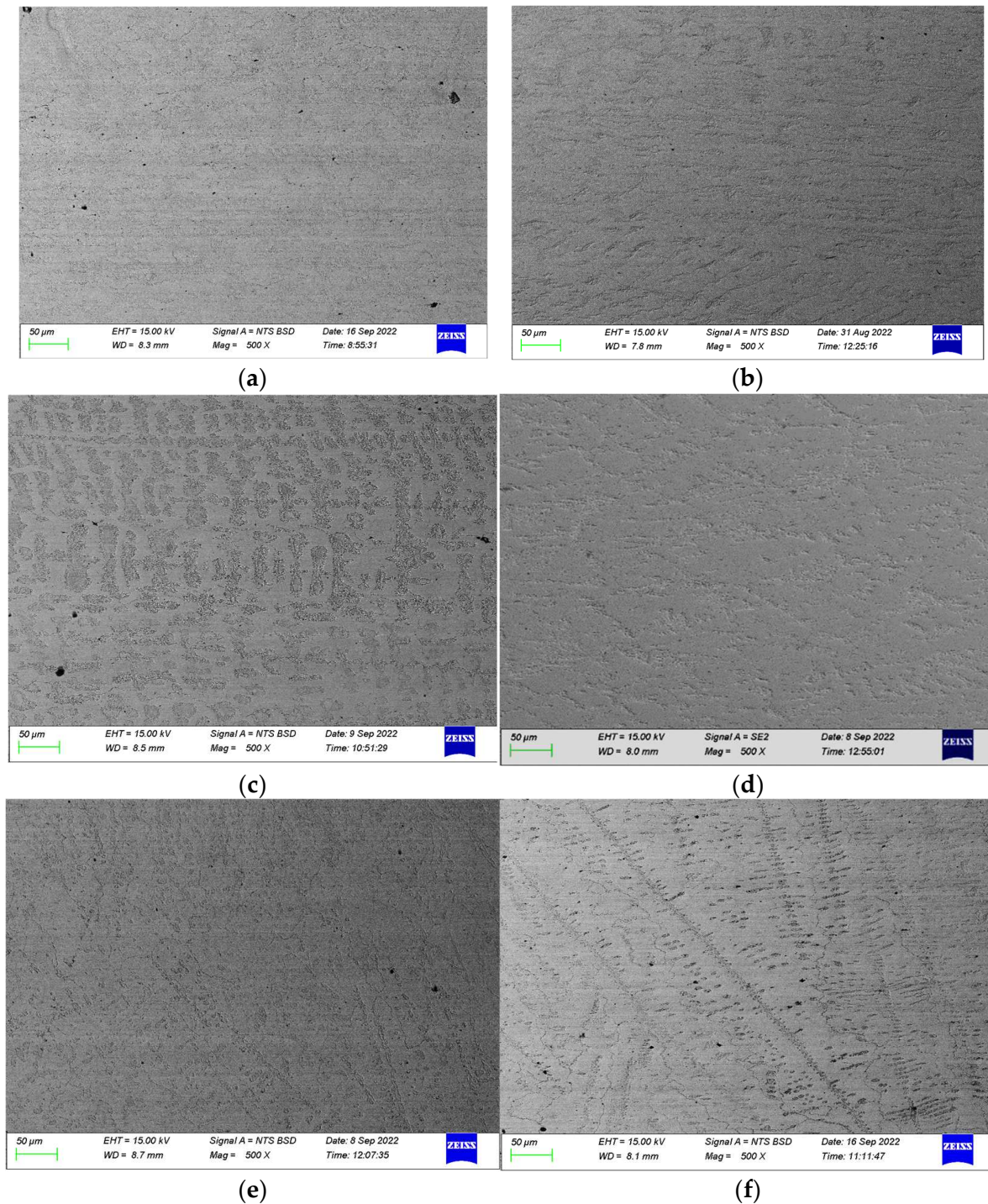
SEM images of deformed Fe-30.9Mn-4.9Al-4.5Cr-0.4C and Fe-21.3Mn-7.6Al-4.3Cr-1C low-density steels are presented in Figures 10 and 11, respectively. The SEM images were taken in either back-scattered electron or secondary electron imaging mode at  $500\times$  magnification. The elongated and globular ferrite phase that was mentioned in Section 3.3.1 can be observed in the Fe-30.9Mn-4.9Al-4.5Cr-0.4C austenitic-based duplex low-density steel under all deformation conditions (Figure 10), except at 1000 °C at  $0.1 \text{ s}^{-1}$  (Figure 10e) where the ferrite phase dissolved into the austenite and carbides seen at the austenite boundaries. Dendritic configurations that were dominant in the as-cast condition were not seen in Figure 11. However, for the austenitic Fe-21.3Mn-7.6Al-4.3Cr-1C low-density steel (Figure 11), dendritic features were seen in samples deformed at 1000 °C at  $5 \text{ s}^{-1}$  (Figure 11e). At 800 °C at  $0.1 \text{ s}^{-1}$ , 800 °C at  $5 \text{ s}^{-1}$ , 900 °C at  $5 \text{ s}^{-1}$ , and 1000 °C at  $0.1 \text{ s}^{-1}$  (Figure 11a,b,d,e), the carbides were distributed within the matrix and around the austenite boundaries. Only at 900 °C at  $0.1 \text{ s}^{-1}$  (Figure 11c) did the carbides form a rounded or petal-like feature within the matrix. These features were evenly distributed within the austenite matrix.



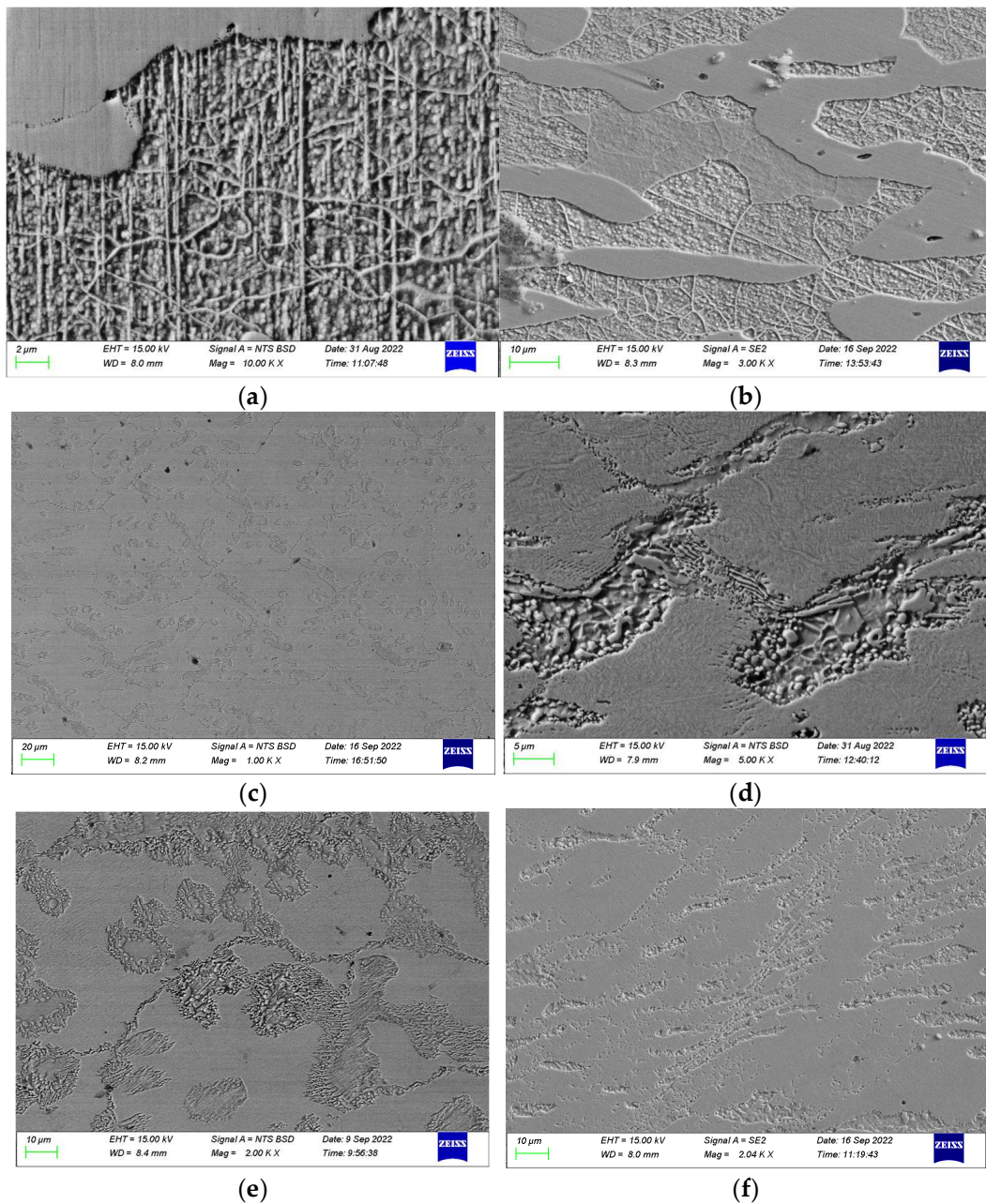
**Figure 10.** Scanning electron microscope images of deformed Fe-30.9Mn-4.9Al-4.5Cr-0.4C under different deformation conditions: (a) 800 °C at 0.1 s<sup>-1</sup>; (b) 800 °C at 5 s<sup>-1</sup>; (c) 900 °C at 0.1 s<sup>-1</sup>; (d) 900 °C at 5 s<sup>-1</sup>; (e) 1000 °C at 0.1 s<sup>-1</sup>; (f) 1000 °C at 5 s<sup>-1</sup>.

Figure 12 shows selected SEM images of deformed Fe-30.9Mn-4.9Al-4.5Cr-0.4C and Fe-21.3Mn-7.6Al-4.3Cr-1C low-density stainless steels taken at higher magnification. Apart from the elongated and globular ferrite phase, equiaxed grains were visible in the austenitic region of the duplex low-density Fe-30.9Mn-4.9Al-4.5Cr-0.4C stainless steel (Figure 12a,b). These equiaxed grains are signatures of DRX [25,26]. Furthermore, carbide particles were seen within the equiaxed grains. This suggests that the duplex low-density steel consisted of ferrite and austenite + carbide phases. However, this was not the case at 1000 °C at 0.1 s<sup>-1</sup>, where the phase constituent was predominantly an austenite matrix with embedded carbides around the austenite grains (Figure 12c). For the austenitic Fe-21.3Mn-7.6Al-4.3Cr-1C low-density steel (Figure 12d,e), the carbides were seen within and around the austenite boundaries. At 1000 °C at 5 s<sup>-1</sup> (Figure 12f), most of the carbides maintained the dendritic configuration, but at 900 °C at 0.1 s<sup>-1</sup> (Figure 12e), the carbides had a rounded morphology, suggesting that there was some degree of dynamic globularization. Unlike in

the duplex low-density steel, there was no evidence of an equiaxed austenite grain in this alloy and, as such, dynamic recovery was the dominant softening mechanism under the deformation conditions.



**Figure 11.** Scanning electron microscope images of deformed Fe-21.3Mn-7.6Al-4.3Cr-1C under different deformation conditions: (a) 800 °C at 0.1 s<sup>-1</sup>; (b) 800 °C at 5 s<sup>-1</sup>; (c) 900 °C at 0.1 s<sup>-1</sup>; (d) 900 °C at 5 s<sup>-1</sup>; (e) 1000 °C at 0.1 s<sup>-1</sup>; (f) 1000 °C at 5 s<sup>-1</sup>.



**Figure 12.** Higher-magnification-scanning electron images of deformed Fe-30.9Mn-4.9Al-4.5Cr-0.4C at (a) 800 °C at 0.1 s<sup>-1</sup>; (b) 1000 °C at 5 s<sup>-1</sup>; (c) 1000 °C at 0.1 s<sup>-1</sup> and Fe-21.3Mn-7.6Al-4.3Cr-1C at (d) 800 °C at 5 s<sup>-1</sup>; (e) 900 °C at 0.1 s<sup>-1</sup>; (f) 1000 °C at 5 s<sup>-1</sup>.

#### 4. Discussion

The two low-density steels, Fe-30.9Mn-4.9Al-4.5Cr-0.4C and Fe-21.3Mn-7.6Al-4.3Cr-1C, considered in this study were identified as austenite-based duplex low-density steel and austenitic low-density steel, respectively. Their composition and initial microstructures are consistent with the classification prescribed by Chen et al. [4]. The interest in these alloys stemmed from their potential to be used as alternative bio-implant materials given their lower corrosion rates in simulated body fluids compared to commercial-grade 316L stainless steel [10]. Similar to Fe-Mn-Al-Cr-C low-density steel subjected to corrosion investigation in NaCl and NaOH in a previous study [11], pitting corrosion was observed in the two alloys that were considered in this study. However, the location of the pits differed. In previous work, the shallow and tiny pits formed on all phases in the alloy, whereas the deep pits

in these alloys formed preferentially at the inter-dendritic regions due to the dissolution of the austenite–carbide interface, resulting in the pullout of carbide particles [10]. To address this problem, we hypothesized that breaking the dendritic structures in both alloys using thermomechanical processing routes would help redistribute the alloying elements, eliminate segregation, and ultimately reduce the susceptibility of the alloys to pitting corrosion. However, the response of the alloys to hot working parameters is unknown as they have unique compositions that have not been subjected to hot working investigations previously. Additionally, previous studies on the hot working of Fe-Mn-Al-C low-density steels have only been on alloys subjected to either heat treatment or some form of forging or rolling prior to hot working experiments [15,16,25]. Therefore, the initial microstructure of the hot-worked Fe-Mn-Al-C low-density steels reported in the literature differs from the dendritic structure that was the focus of this work. In this study, the alloys were in the as-cast condition, and it is important to establish the most appropriate deformation conditions for breaking the alloys' dendritic structure. While the ultimate goal is to improve resistance to pitting corrosion in these alloys through microstructural control, the thrust of this study was to understand how the two low-density stainless steels respond to imposed hot working conditions.

The hot working parameters considered here were selected from previous studies on the hot working of Fe-Mn-Al-C low-density steels [14,25]. This approach differs from the common practice in previous studies [14,15] where a wide range of strain rates and deformation temperatures were selected to establish the safe and unsafe working regime for a specific alloy. While the parameters selected for the alloys were typical safe working regimes for many Fe-Mn-Al-C low-density steels [14,15,25], we assessed if these parameters would be suitable for hot working of the two alloys investigated in this study. If suitable, defects such as voids, cracking, incipient melting, and adiabatic shear bands are not expected in the alloys after deformation. Although the continuous flow softening seen in the flow curves (Figure 5b) under specific working conditions (800 and 900 °C at 0.1 s<sup>-1</sup>) suggest the occurrence of either deformation-induced cracking or dynamic globularization during deformation [18], the microstructural evidence showed that continuous flow softening was caused by dynamic globularization (Figure 8a,c). No cracking or other defects were seen in the deformed samples of the two alloys. This confirmed that the safe hot working parameters selected from previous works are indeed suitable for the hot working of Fe-30.9Mn-4.9Al-4.5Cr-0.4C and Fe-21.3Mn-7.6Al-4.3Cr-1C low-density stainless steels.

From the flow behavior of the alloys in Figure 5, flow oscillations were dominant on the stress–strain curves when hot working was carried out at a strain rate of 0.1 s<sup>-1</sup>. These oscillations were not seen at 5 s<sup>-1</sup>; rather, a steady-state-flow stress was dominant. These trends suggest the occurrence of DRX and dynamic recovery during deformation of the alloys at these respective strain rates. Previous studies [31,32] on low-density steels have shown that DRX and dynamic recovery are some of the common softening mechanisms in hot-worked low-density steels, and their occurrence depends on certain combinations of strain rate and temperatures.

To identify the deformation conditions that favor DRX and dynamic recovery during hot working of the two alloys, the microstructural features in the as-cast and deformed samples were compared. The as-cast microstructure of the duplex Fe-30.9Mn-4.9Al-4.5Cr-0.4C low-density stainless steel contained predominantly dendritic ferrite and austenite, while the austenitic-based low-density steel had carbides with dendritic configuration. The dendritic ferrite and austenite evolved to elongated and globular austenite in the duplex low-density steel at temperatures below 1000 °C regardless of the strain rates. The globular and elongated ferrite phase appeared as islands within the austenitic matrix. However, at 1000 °C, the strain rate influenced the dendritic microstructure. For the duplex low-density steel, hot working at 1000 °C and 5 s<sup>-1</sup> resulted in elongated and globular ferrite such as those deformed at lower temperatures. The globular ferrite confirmed that one of the softening mechanisms of the alloy is dynamic globularization. However, when higher-magnification SEM images were taken in the austenitic region (Figure 12), the presence

of equiaxed austenite grains confirmed the occurrence of DRX as an additional softening mechanism. In contrast, hot-worked duplex low-density steel showed no ferrite phase, and there was no evidence of dynamically recrystallized grains at 1000 °C at 0.1 s<sup>-1</sup>. It can be concluded that both DRX of the austenitic phase and dynamic globularization of the ferrite phase contributed to the softening of the duplex low-density stainless steel when hot-worked at 800 °C at 0.1 s<sup>-1</sup>, 800 °C at 5 s<sup>-1</sup>, 900 °C at 0.1 s<sup>-1</sup>, 900 °C at 5 s<sup>-1</sup>, and 1000 °C at 5 s<sup>-1</sup>, while the dominant softening mechanism at 1000 °C at 0.1 s<sup>-1</sup> was dynamic recovery. Higher deformation temperatures and low strain rates allow for thermal softening with enough time for atom diffusion and grain boundary migration, favoring dynamic recovery [26].

For the austenitic Fe-21.3Mn-7.6Al-4.3Cr-1C low-density stainless steel, the dendritic carbide in the as-cast condition was redistributed within and around the austenite grains at deformation temperatures below 1000 °C and strain rates of 0.1 and 5 s<sup>-1</sup>. More elongated austenite grains were serrated and a few austenite globules were visible. This confirms dynamic recovery as the dominant softening mechanism despite some occurrence of dynamic globularization. The hot-worked austenitic low-density steel showed a different response at 1000 °C and different strain rates. The dendritic structure remained at 1000 °C at 5 s<sup>-1</sup>, while at 1000 °C at 0.1 s<sup>-1</sup>, the carbides were redistributed within and around the austenite grain as observed when deforming at lower deformation temperatures. It can be concluded that hot-working low-density steel at 1000 °C at 5 s<sup>-1</sup> was ineffective in breaking down as-cast dendritic carbides in the alloy.

Due to macro- and micro-segregation arising from significant alloying elements, different carbides may form in low-density steels [4]; however, XRD only confirmed the M<sub>7</sub>C<sub>3</sub> carbide type. Even M<sub>23</sub>C<sub>6</sub> predicted by Thermo-Calc was not confirmed experimentally. Kappa carbides expected in austenitic Fe-21.3Mn-7.6Al-4.3Cr-1C low-density stainless steels due to the high Al and C content [4] were also not identified. The type of carbide that evolved after hot working is unknown; thus, future work will focus on the evolution of carbides in hot-worked alloys. As breaking down the as-cast dendritic structure was achieved under certain deformation conditions, it is important to evaluate the pitting corrosion resistance of the deformed alloys compared to the as-cast samples in simulated body fluids. This is being investigated by our research group. The hardness results (Figure 7) indicate that hot working improved the hardness of the two low-density stainless steels compared to the as-cast dendritic structure. This can be ascribed to grain refinement and carbide redistribution in the alloys. Wang et al. [31] reported that grain refinement was caused by DRX in hot-worked Fe-30Mn-11Al-1C-0.1Nb-0.1V alloy at relatively low deformation temperatures (850 to 950 °C) and strain rates of 1 to 10 s<sup>-1</sup>. Their alloy's refined grains and hardness were sensitive to deformation temperatures and strain rates. Higher deformation temperatures and low strain rates caused an increase in the average grain size of the austenite grains, decreasing the hardness. Although, in our work, grain refinement and microstructural reconstitution are prominent at 800 and 900 °C as in Wang et al. [31], the hardness increased slightly with deformation temperature and was insensitive to increasing strain rate. The discrepancy between this work and that of Wang et al. [31] can be attributed to the difference in alloy compositions, as well as different initial microstructures. Furthermore, Churyumov et al. [32] established that grain refinement was optimum at a deformation temperature of 1050 °C and 10 s<sup>-1</sup> strain rate in hot-worked Fe-35Mn-10Al-1C steel. The disagreement between the optimum deformation temperature for grain refinement in our work, Wang et al. [31], and Churyumov et al. [32] implies that the different compositions and initial microstructures influence the response of low-density steels to deformation parameters. Therefore, alloys with unique compositions must be subjected to various testing conditions to understand their behavior.

## 5. Conclusions

Hot working is an effective technique for shaping and achieving microstructural control in metallic alloys. However, the most advantageous parameters to achieve the desired microstructure and properties must be established to improve product performance. In addition, these parameters are important for producing semi-finished and finished components with reproducible microstructures and properties. In this study, the combination of parameters for breaking as-cast dendritic structures in two grades of low-density stainless steels, Fe-30.9Mn-4.9Al-4.5Cr-0.4C and Fe-21.3Mn-7.6Al-4.3Cr-1C, was investigated. There is rarely any study considering the hot working of Fe-Mn-Al-C low-density steel with initial dendritic microstructure. Understanding the relationship between deformation parameters and microstructural evolution could enhance processing steps and improve alloys' overall performance. Based on this study's results, the following conclusions are made:

- (1) The flow behavior of the two alloys, Fe-30.9Mn-4.9Al-4.5Cr-0.4C and Fe-21.3Mn-7.6Al-4.3Cr-1C, was generally similar to that of most metallic alloys with positive strain rate sensitivity because flow stress increased with decreasing deformation temperatures and increasing strain rate.
- (2) The complete breakdown of dendritic features can be achieved at deformation temperatures of 800 and 900 °C and strain rates of 0.1 and 5 s<sup>-1</sup> in both alloys.
- (3) The breakdown of dendritic structure at 1000 °C was dependent on strain rate, especially in the austenitic-grade Fe-21.3Mn-7.6Al-4.3Cr-1C low-density stainless steel where 0.1 s<sup>-1</sup> was effective, but 5 s<sup>-1</sup> retained the dendritic structure.
- (4) Dynamic globularization of ferrite and DRX of austenite grains were identified as the dominant softening mechanisms in duplex Fe-30.9Mn-4.9Al-4.5Cr-0.4C low-density stainless steel except at 1000 °C at 0.1 s<sup>-1</sup> where dynamic recovery dominated.
- (5) Dynamic recovery controlled the softening of austenitic-based Fe-21.3Mn-7.6Al-4.3Cr-1C low-density stainless steel, but few globular austenites were seen at 800 and 900 °C, indicating that some dynamic globularization still occurred.
- (6) Hot working under all conditions improved the hardness of both alloys owing to the reconstitution and refinement of the microstructural constituents.

**Supplementary Materials:** The following supporting information can be downloaded at: <https://www.mdpi.com/article/10.3390/app13042310/s1>, Figure S1: Pitting corrosion in the dendritic region of low-density stainless steel.

**Author Contributions:** T.K. conducted the experimental analysis and wrote the first draft of the manuscript; N.M. co-supervised the work and contributed to funding acquisition; D.K. co-conceptualized and co-supervised the study, contributed to funding acquisition, writing, reviewing, and editing the manuscript; J.v.d.M. co-supervised and contributed to funding acquisition; M.B. co-conceptualized and supervised the study, and contributed to funding acquisition as the principal applicant, writing, reviewing, and editing the manuscript. All authors have read and agreed to the published version of the manuscript.

**Funding:** This research was funded by the Faculty Research Council of the University of the Witwatersrand, South Africa.

**Institutional Review Board Statement:** Not applicable.

**Informed Consent Statement:** Not applicable.

**Data Availability Statement:** The raw data obtained from the experiments will be made available on request to readers.

**Acknowledgments:** The authors acknowledge Vuyo Clifford Motsweni of MINTEK, who is now late, for his assistance with casting the alloys.

**Conflicts of Interest:** The authors declare no conflict of interest. The funders had no role in the design of the study; in the collection, analyses, or interpretation of data; in the writing of the manuscript; or in the decision to publish the results.

## References

1. Chen, S.; Rana, R. Low-density steels. In *High-Performance Ferrous Alloys*; Rana, R., Ed.; Springer: Berlin/Heidelberg, Germany, 2021; pp. 211–289. [CrossRef]
2. Kalantari, A.-R.; Zarei-Hanzaki, A.; Abedi, H.R.; Jalali, M.S.; Park, S.-J.; Park, J.Y. The high temperature deformation behavior of a triplex (ferrite+ austenite+ martensite) low-density steel. *J. Mater. Res. Technol.* **2021**, *13*, 1388–1401. [CrossRef]
3. Gutierrez-Urrutia, I. Low-density Fe-Mn-Al-C steels: Phase structures, mechanisms and properties. *ISIJ Int.* **2021**, *61*, 16–25. [CrossRef]
4. Chen, S.; Rana, R.; Haldar, A.; Ray, R.K. Current state of Fe-Mn-Al-C low-density steels. *Prog. Mater. Sci.* **2017**, *89*, 345–391. [CrossRef]
5. Moon, J.; Ha, H.-Y.; Kim, K.-W.; Park, S.-J.; Lee, T.-H.; Kim, S.-D.; Jang, J.H.; Jo, H.-H.; Hong, H.-U.; Lee, B.H.; et al. A new class of lightweight, stainless steels with ultra-high strength and large ductility. *Sci. Rep.* **2020**, *10*, 12140. [CrossRef]
6. Di Schino, A. Manufacturing and applications of stainless steels. *Metals* **2020**, *10*, 327. [CrossRef]
7. Disegi, J.A.; Eschbach, L. Stainless steel in bone surgery. *Injury* **2000**, *31* (Suppl. S4), 2–6. [CrossRef] [PubMed]
8. Talha, M.; Behera, C.K.; Sinha, O.P. A review on nickel-free nitrogen containing austenitic stainless steels for biomedical applications. *Mater. Sci. Eng. C.* **2013**, *33*, 3563–3575. [CrossRef] [PubMed]
9. Gotman, I. Characteristics of metals used in implants. *J. Endourol.* **1997**, *11*, 383–389. [CrossRef]
10. Bodunrin, M.O.; Dladla, A.; Rundora, N.; Klenam, D.E.P. Corrosion behavior of austenitic low-density stainless steels in simulated body fluids. In Proceedings of the Microscopy Society of Southern African Conference, Johannesburg, South Africa, 5–8 December 2022; p. 92. Available online: [https://www.microscopy.co.za/file/638db0f360846/mssa\\_2022-proceedings.pdf](https://www.microscopy.co.za/file/638db0f360846/mssa_2022-proceedings.pdf) (accessed on 1 February 2023).
11. Bosch, J.; Martin, U.; Aperador, W.; Bastidas, J.M.; Ress, J.; Bastidas, D.M. Corrosion behavior of high-Mn austenitic Fe–Mn–Al–Cr–C steels in NaCl and NaOH solutions. *Materials* **2021**, *14*, 425. [CrossRef]
12. Ding, H.; Liu, D.; Cai, M.; Zhang, Y. Austenite-based Fe-Mn-Al-C lightweight steels: Research and prospective. *Metals* **2022**, *12*, 1572. [CrossRef]
13. Satyanarayana, D.V.V.; Malakondaiah, G.; Sarma, D.S. Analysis of flow behaviour of an aluminium containing austenitic steel. *Mater. Sci. Eng. A.* **2007**, *452–453*, 244–253. [CrossRef]
14. Liu, D.; Ding, H.; Cai, M.; Han, D. Hot deformation behavior and processing map of a Fe-11Mn-10Al-0.9C duplex low-density steel susceptible to  $\kappa$ -Carbides. *J. Mater. Eng. Perform.* **2019**, *28*, 5116–5126. [CrossRef]
15. Mohamadizadeh, A.; Zarei-Hanzaki, A.; Abedi, H.R.; Mehtone, S.; Porter, D. Hot deformation characterization of duplex low-density steel through 3D processing map development. *Mater. Charact.* **2015**, *107*, 293–301. [CrossRef]
16. ASTM International. ASTM E92–17. Available online: <https://www.astm.org/e0092-17.html> (accessed on 1 February 2023).
17. Abioye, T.E.; Farayibi, P.K.; Clare, A.T. A comparative study of Inconel 625 laser cladding by wire and powder feedstock. *Mater. Manuf. Process.* **2017**, *32*, 1653–1659. [CrossRef]
18. Bodunrin, M.O.; Chown, L.H.; van der Merwe, J.W.; Alaneme, K.K. Hot working behaviour of experimental Ti-4.5Al-1 V-3Fe alloy with initial lamellar microstructure. *Int. J. Adv. Manuf. Technol.* **2020**, *106*, 1901–1916. [CrossRef]
19. De Sousa Sulzbach, G.A.; Rodrigues, M.V.G.; Rodrigues, S.F.; Macedo, G.M.E.; de Abreu, H.F.G.; Aranas, C.; Reis, G.S.; Silva, E.S. Constitutive analysis of stress–strain curves in dynamic softening of high Nb- and N-containing austenitic stainless-steel biomaterial. *J. Mater. Res. Technol.* **2022**, *19*, 4939–4956. [CrossRef]
20. Devincere, B.; Hoc, T.; Kubin, L. Dislocation mean free paths and strain hardening of crystals. *Science* **2008**, *320*, 1745–1748. [CrossRef]
21. Marchattiar, A.; Sarkar, A.; Chakravartty, J.K.; Kashyap, B.P. Dynamic recrystallization during hot deformation of 304 austenitic stainless steel. *J. Mater. Eng. Perform.* **2013**, *22*, 2168–2175. [CrossRef]
22. Huang, K.; Logé, R.E. A review of dynamic recrystallization phenomena in metallic materials. *Mater. Des.* **2016**, *111*, 548–574. [CrossRef]
23. Luton, M.J.; Sellars, C.M. Dynamic recrystallization in nickel and nickel-iron alloys during high temperature deformation. *Acta Metall.* **1969**, *17*, 1033–1043. [CrossRef]
24. Sakai, T.; Jonas, J.J. Overview no. 35 Dynamic recrystallization: Mechanical and microstructural considerations. *Acta Metall.* **1984**, *32*, 189–209. [CrossRef]
25. Sun, J.; Li, J.; Wang, P.; Huang, Z. Hot deformation behavior, dynamic recrystallization and processing map of Fe–30Mn–10Al–1C low-density steel. *Trans. Indian Inst. Met.* **2022**, *75*, 699–716. [CrossRef]
26. Bodunrin, M.O.; Chown, L.H.; van der Merwe, J.W.; Alaneme, K.K. Microstructural evolution during hot forming of Ti-6Al-4V alloy with complex initial microstructure. *Int. J. Adv. Manuf. Technol.* **2019**, *104*, 3017–3026. [CrossRef]
27. Rodrigues, S.F.; Silva, E.S.; Reis, G.S.; de Sousa, R.C.; Balancin, O. Prediction of hot flow plastic curves of ISO 5832-9 steel used as orthopedic implants. *Mater. Res.* **2014**, *17*, 436–444. [CrossRef]
28. Son, H.-W.; Lee, J.-W.; Hyun, S.-K. Mechanism of grain boundary serration during hot deformation of AZ31 alloy: Role of grain boundary dislocations and grain boundary sliding. *Int. J. Plast.* **2020**, *125*, 118–132. [CrossRef]
29. Zhu, Y.C.; Zeng, W.D.; Liu, J.L.; Zhao, Y.Q.; Zhou, Y.G.; Yu, H.Q. Effect of processing parameters on the hot deformation behavior of as-cast TC21 titanium alloy. *Mater. Des.* **2012**, *33*, 264–272. [CrossRef]

30. Fan, J.K.; Kou, H.C.; Lai, M.J.; Tang, B.; Chang, H.; Li, J.S. Hot deformation mechanism and microstructure evolution of a new near  $\beta$  titanium alloy. *Mater. Sci. Eng. A* **2013**, *584*, 121–132. [[CrossRef](#)]
31. Wang, H.; Gao, Z.; Shi, Z.; Xu, H.; Zhang, L.; Wu, G.; Wang, C.; Wang, C.; Weng, Y.; Cao, W. High temperature deformation behavior and microstructure evolution of low-density steel Fe30Mn11Al1C micro-alloyed with Nb and V. *Mater.* **2021**, *14*, 6555. [[CrossRef](#)]
32. Churyumov, A.Y.; Kazakova, A.A.; Pozdniakov, A.V.; Churyumova, T.A.; Prosviryakov, A.S. Investigation of hot deformation behavior and microstructure evolution of lightweight Fe-35Mn-10Al-1C steel. *Metals* **2022**, *12*, 831. [[CrossRef](#)]

**Disclaimer/Publisher’s Note:** The statements, opinions and data contained in all publications are solely those of the individual author(s) and contributor(s) and not of MDPI and/or the editor(s). MDPI and/or the editor(s) disclaim responsibility for any injury to people or property resulting from any ideas, methods, instructions or products referred to in the content.